Impact of Spin-Wave Dispersion on Surface-Acoustic-Wave Velocity

Pauline Rovillain,[1,*] Jean-Yves Duquesne,[1] Louis Christienne,[1] Mahmoud Eddrief,[1] Maria Gloria Pini,[2] Angelo Rettori,[3,4] Silvia Tacchi,[5] and Massimiliano Marangolo[1]

[1] *Sorbonne Université, CNRS, Institut des NanoSciences de Paris, INSP, UMR7588, F-75005 Paris, France*
[2] *Istituto dei Sistemi Complessi del CNR (CNR-ISC), Sede Secondaria di Firenze, I-50019 Sesto Fiorentino, Italy*
[3] *Dipartimento di Fisica ed Astronomia, Universitá degli Studi di Firenze, I-50019 Sesto Fiorentino, Italy*
[4] *INFN, Sezione di Firenze, I-50019 Sesto Fiorentino, Italy*
[5] *Istituto Officina dei Materiali del CNR (CNR-IOM), Sede Secondaria di Perugia, c/o Dipartimento di Fisica e Geologia, Universitá di Perugia, I-06123 Perugia, Italy*

(Received 28 March 2022; revised 2 November 2022; accepted 9 November 2022; published 15 December 2022)

The dependence of the velocity of surface acoustic waves (SAWs) as a function of an external applied magnetic field is investigated in a Fe thin film epitaxially grown on a piezoelectric GaAs substrate. The SAW velocity is observed to strongly depend on both the amplitude and direction of the magnetic field. To interpret the experimental data a phenomenological approach to the relative change in SAW velocity is implemented. We find that the experimental velocity variation can be well reproduced provided that the spin-wave dispersion is taken into account. The validity of this phenomenological model is attested by the comparison with a fully magnetoelastic one. Nonreciprocity of SAW velocity is also addressed both experimentally and theoretically.

DOI: 10.1103/PhysRevApplied.18.064043

I. INTRODUCTION

In recent years, the coupling between surface acoustic waves (SAWs) and spin waves (SWs) [1] in magnetic films has been the subject of increasing interest due to its possible application in the framework of magnonics [2,3]. The latter research field aims to process information at low power consumption, small footprint, and high operation speed in a wide frequency range from gigahertz to terahertz. In this context, SAWs have been proposed to dynamically control SW propagation and even to generate SWs, in order to implement reconfigurable and energy-efficient magnonic devices [3]. Indeed, SAW technology is mature and widely used in today's sensors, filters, and microwave circuitry, notwithstanding the lack of tunability of SAW transducers. For this reason a multitude of them are currently integrated in modern devices (e.g., mobile phones). In this context, it has been shown that tunability can be increased by using electric [4] or magnetic [5] fields.

Recently, the so-called SAW-induced ferromagnetic resonance (SAW FMR) has been observed by Weiler *et al.* [6], Thevenard *et al.* [7], and Duquesne *et al.* [8] in Ni, GaMnAs and Fe thin films, respectively, by exciting SAWs in the gigahertz and subgigahertz regime in piezoelectric media. Moreover, it is worth noticing that SAW FMR permits one to reverse magnetization [9] and even to induce spin-pumping in CoPt bilayers [10,11].

The SAW-FMR interaction is often described [12] by taking into account only the uniform FMR mode (i.e., $k_{SW} = 0$). However, this approximation is rather crude, and it misses out the wealth of modes that can be excited in a ferromagnetic (FM) material. Moreover, when compared to other waves (photons, phonons, etc.), SWs present two important features: their frequency can be easily varied by applying an external magnetic field $\mathbf{B}_{ext}$, and their dispersion curves strongly depend on the direction of $\mathbf{B}_{ext}$ with respect to the SW wavevector $\mathbf{k}$. Because of long-range magnetic dipole-dipole interactions, SWs at low wavevectors present negative (positive) group velocity when the magnetization is parallel (perpendicular) to the $\mathbf{k}$-vector, corresponding to the so-called backward (BA) [Damon-Eshbach (DE)] configuration [13]. Therefore, the in-plane anisotropy of SWs dispersion has to be taken into account for the design of magnonic devices where SAWs are exploited to control or generate SWs. Interestingly, some recent articles evidence the important role played by a nonzero wavevector [14–19].

In particular, Babu *et al.* studied the SAW-SW coupling by Brillouin light scattering (BLS) in a wide range of $\mathbf{k}$-values [16]. They showed that in order to obtain an appreciable coupling between SWs and SAWs, the SAW profile within the magnetostrictive layer is also of

*pauline.rovillain@insp.upmc.fr

importance [16], in addition to the anisotropy of the magnetoelastic interaction with respect to the orientation of the magnetic field [12].

In our previous work [8] we have shown that SAW FMR can be obtained in an epitaxial Fe thin film by monitoring attenuation and velocity changes of the SAWs. Here, we investigate the dependence of the SAW velocity variation $\Delta V/V$ as a function of the in-plane direction of the external applied magnetic field $\mathbf{B}_{\text{ext}}$. We find that $\Delta V/V$ strongly depends on the orientation between $\mathbf{B}_{\text{ext}}$ and the SAW wavevector ($\mathbf{k}_{\text{SAW}}$). In particular, we show that in order to well reproduce and interpret the experimental results, the SWs dispersion has to be included in the theoretical model. Our approach is an extension of the model given by Dreher *et al.* [12] to describe the back action of the ferromagnetic resonance on the acoustic wave. In the literature, this phenomenological model has been adopted to quantify the part of the SAW power used to drive the magnetization dynamics by considering SAW propagation and FMR in the ferromagnetic thin film, that is, by neglecting SAW propagation in the substrate [8,12,15]. Here, we show that the back-action model is also able to catch the physics of SAW velocity changes in a ferromagnetic thin film. Moreover, we corroborate this approximate approach by a comparison with a more sophisticated calculation (i.e., a fully magnetoelastic approach) which considers SAW propagation in the heterostructure as a whole, composed of the thin magnetic layer on a substrate.

A full comprehension of SAW-SW interaction opens up dazzling Janus-faced applications. On the one hand, a single interdigitated transducer can provide the energy needed to activate magnetization dynamics in a Joule heat-free manner. On the other hand, the too limited phase and/or resonance frequency tunability in SAW filters can be augmented by an external magnetic field, as shown by Zhou *et al.* [5].

II. SAMPLE CHARACTERISTICS AND EXPERIMENTAL SETUP

A single-crystal Fe thin film with a thickness of 54 nm [20] was deposited on a ZnSe(001) epilayer (approximately 20 nm thick) grown on GaAs(001) substrate. An Au capping layer (approximately 8 nm thick) was deposited to protect the Fe thin film. The layer thickness was determined by TEM and x-ray reflectivity. The heterostructure exhibits the expected epitaxial growth relationship, which is [100]Fe‖[100]ZnSe‖[100]GaAs and (001)Fe‖(001)ZnSe‖(001)GaAs. In agreement with previous work [21], vibrating sample magnetometer measurements show that the sample is characterized by in-plane biaxial magnetic anisotropy, typical of bulk Fe, with the magnetic easy and hard axis along the [100] and [110] directions, respectively. Details of the growth, characterization, and magnetic properties of Fe thin films are given in Ref. [8]. Then a 4×4 mm^2 mesa is defined by ion etching in order to perform acoustic measurements. SAWs were excited along the [110] direction ($\mathbf{k}_{\text{SAW}}$‖[110]) at four harmonic frequencies $\nu_{\text{SAW}} \approx q\nu$, with $\nu = 119$ MHz and $q = 1, 3, 5, 7$, by a "split-44" interdigitated transducer (IDT) [22]. An identical IDT acts as a detector. The $\mathbf{k}_{\text{SAW}}$ direction can be reversed by connecting the input signal to one IDT or the other. Pulsed excitation of 500 ns duration was used and the acoustic signal is acquired with a digital oscilloscope to make direct time domain measurements [23]. The device is sketched in Fig. 1. Prior to each measurement, the sample was saturated by a large in-plane external reference magnetic field $\mathbf{B}_{\text{ext}}$, having magnitude $B_{\text{ref}} = 0.4$ T and forming an angle ψ with the [110] direction. The change of the relative SAW velocity $\Delta V/V = [V(B_{\text{ext}}) - V(B_{\text{ref}})]/V(B_{\text{ref}})$ was obtained by measuring the phase of the acoustic signals [24].

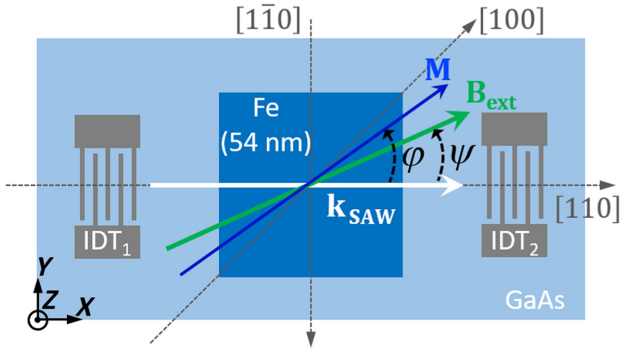

FIG. 1. Sketch of the sample: 4×4 mm^2 Fe mesa (54 nm thick) on GaAs(001). The IDT has a split-44 design [22]. The wavevector $\mathbf{k}_{\text{SAW}}$ is parallel to [110], $\mathbf{B}_{\text{ext}}$ is the in-plane applied magnetic field, and $\mathbf{M}$ is the Fe magnetization.

Before discussing the experimental results, it is useful to analyze the dependence of the lowest- frequency SW mode as a function of the intensity of the magnetic field $\mathbf{B}_{\text{ext}}$ applied along different in-plane directions for a Fe film 54 nm thick. Figures 2(a)–2(c) report the SWs frequency calculated at $k_{\text{SW}} = 0$ and $k_{\text{SW}} = k_{\text{SAW}} = 1.824$ μm^{-1} (i.e., the $\mathbf{k}$-vector of a SAW with frequency $\nu_{\text{SAW}} = 833$ MHz), by means of the model described in Sec. III B, and using the magnetic parameters obtained from the analysis of the broadband-FMR (BB-FMR) and BLS measurements reported in Appendix B [25]. Calculations were performed for $\mathbf{B}_{\text{ext}}$ applied parallel to the [110], [100] and [1$\bar{1}$0] directions, at an angle $\psi = 0°$, 45° and 90° to $\mathbf{k}_{\text{SAW}}$, respectively.

Note that $\psi = 0°$ and $\psi = 90°$ correspond to the BA and DE geometry, where $\mathbf{k}_{\text{SW}}$ is parallel and perpendicular to the sample magnetization, respectively. Figures 2(d)–2(f) report SW frequencies calculated in a restricted range of the $\mathbf{B}_{\text{ext}}$ intensity for $k_{\text{SW}} = 0$ and for k_{SW} equal to the k_{SAW} of the four harmonic frequencies

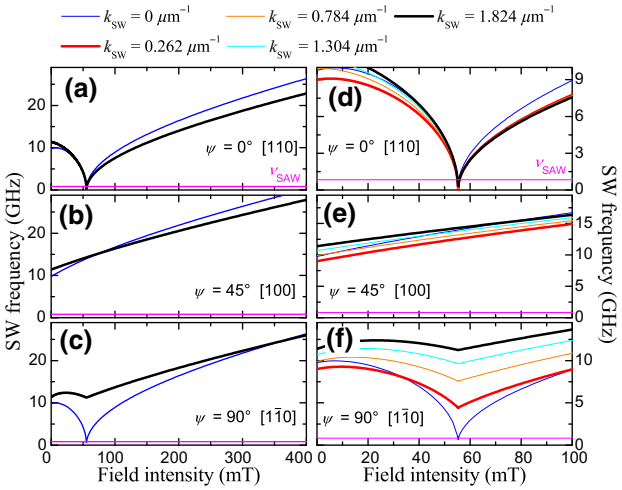

FIG. 2. (a)–(c) SW frequencies versus applied field magnitude, calculated for $k_{SW} = 0$ and $k_{SW} = k_{SAW} = 1.824\ \mu m^{-1}$ in a 54-nm-thick Fe film magnetized in plane, for three different orientations of the external field $\mathbf{B}_{ext}$ applied at angles $\psi = 0°, 45°$, and 90° from $\mathbf{k}_{SAW} \| [\mathbf{110}]$. (d)–(f) Zoom centered around $B_r = 58$ mT of the SW frequencies, calculated for $k_{SW} = 0$ and $k_{SW} = k_{SAW}$, where $k_{SAW} = 0.262, 0.784, 1.304$ and $1.824\ \mu m^{-1}$ are the wavevectors of four SAWs with frequencies 119, 357, 595, and 833 MHz, respectively. The magenta line indicates the SAW frequency excitation at $\nu_{SAW} = 833$ MHz.

ν_{SAW} used in the experiment. These calculations indicate that a wide spectrum of SW excitations can be covered by a simple variation of the ψ-angle.

When the in-plane magnetic field is applied along the [110] and [1$\bar{1}$0] directions, corresponding to $\psi = 0°$ and $\psi = 90°$, respectively, the SW frequency exhibits a nonmonotonic behavior, with a local frequency minimum at an external field of about $B_r \approx 58$ mT; see Figs. 2(a) and 2(c). This is the typical hard-axis behavior, and indicates a reorientation of the sample magnetization. On reducing the strength of the external field, the magnetization does not remain oriented along the hard direction and starts to rotate towards the nearest easy axis (i.e., the in-plane [100] directions), causing the increase in the SW frequency observed for field values smaller than B_r. Moreover, one may note that in the BA configuration the frequency dependence exhibits a marked minimum for all k_{SAW} values, while in the DE configuration the frequency minimum becomes less pronounced on increasing the k_{SAW} magnitude; see Figs. 2(d) and 2(f).

In contrast, when $\mathbf{B}_{ext}$ is parallel to the easy-axis [100] direction (corresponding to $\psi = 45°$), the SW frequency shows a monotonic dependence as a function of B_{ext}; see Figs. 2(b) and 2(e). Since in our experiment ν_{SAW} is smaller than 1 GHz, these calculations indicate that the resonant magnetoelastic coupling effect (RMEC), where both the frequencies and the **k**-vectors of SAW and SW match, can be obtained only in the BA geometry. However, as shown previously in Ref. [8], a slight misalignment of just 0.1° in ψ is capable of driving the system off-resonance because of the rapid increase in the precession frequencies.

III. RESULTS AND DISCUSSION

A. Comparison between different magnetic field directions

Figure 3 reports the velocity changes measured at $\nu_{SAW} = 119$ MHz and 833 MHz, in three different configurations: (a) $\mathbf{B}_{ext} \| [110]$ ($\psi = 0°$); (b) $\mathbf{B}_{ext} \| [100]$ ($\psi = 45°$); and (c) $\mathbf{B}_{ext} \| [1\bar{1}0]$ ($\psi = 90°$). Figure 4 shows more detailed measurements performed at $\psi = 0°$, at the four harmonic frequencies ν_{SAW} and applying the external magnetic field both parallel and antiparallel to the $\mathbf{k}_{SAW}$ direction. It is worth noticing that the velocity change strongly depends on the angle between the direction of $\mathbf{B}_{ext}$ and

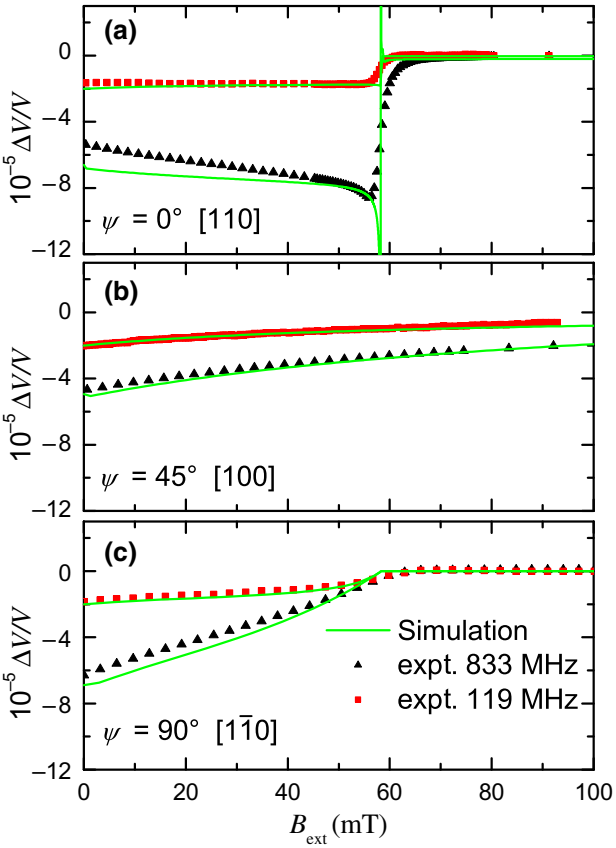

FIG. 3. Relative variation of the SAW velocity V measured versus decreasing amplitude of the external field B_{ext} at $\nu_{SAW} = 119$ MHz and 833 MHz. The magnetic field $\mathbf{B}_{ext}$ is applied in the film plane, parallel (a) to the [110] direction (hard axis, $\psi = 0°$), (b) to the [100] direction (easy axis, $\psi = 45°$), or (c) to the [1$\bar{1}$0] direction (hard axis, $\psi = 90°$). At $\psi = 0°$, $\mathbf{k}_{SAW}$ and $\mathbf{B}_{ext}$ are parallel, with $\mathbf{k}_{SAW}$ parallel to the [110] direction. The lines correspond to the simulation results using the model in Sec. III B, that is, taking into account both the Rayleigh wave and the correct SW dispersion with a Gilbert constant $\alpha = 0.005$.

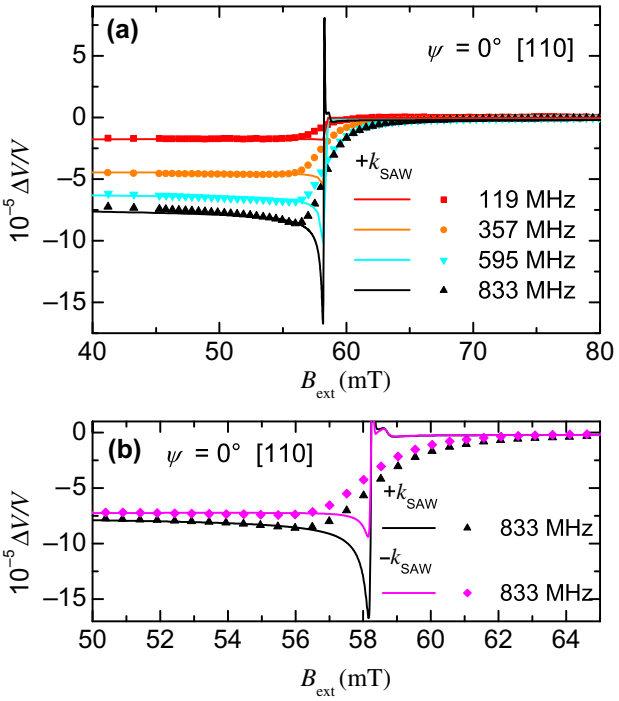

FIG. 4. (a) Relative variation of the SAW velocity V measured versus decreasing amplitude of the external field $\mathbf{B}_{\text{ext}}\|[110]$ (i.e., $\psi = 0°$) at $\nu_{\text{SAW}} = 119$, 357, 595, and 833 MHz. $\mathbf{k}_{\text{SAW}}$ and $\mathbf{B}_{\text{ext}}$ are parallel, with $\mathbf{k}_{\text{SAW}}$ parallel to the [110] direction. The solid lines correspond to the simulation results using the model in Sec. III B. (b) At 833 MHz, both $+\mathbf{k}_{\text{SAW}}$ and $-\mathbf{k}_{\text{SAW}}$ experimental (symbols) and simulation curves (solid lines) are shown and correspond to the SAW propagation direction parallel and antiparallel to [110], respectively.

k_{SAW}. When $\mathbf{B}_{\text{ext}}\|[110]$ the relative variation of SAW velocity presents a sharp change at the saturation magnetic field, B_r, which becomes less pronounced on reducing the SAW frequency. This behavior is a signature of the RMEC conditions as demonstrated in Ref. [8]. In this geometry, indeed, the resonance conditions are fulfilled owing to the dramatic lowering of the SWs frequencies at B_r, as discussed above and presented in Figs. 2(a) and 2(d).

In contrast, a smoother change is observed for the velocity variation when $\mathbf{B}_{\text{ext}}\|[1\bar{1}0]$ [Fig. 3(c)] at both 833 and 119 MHz. In this configuration, the frequency matching (i.e., $\nu_{\text{SAW}} = \nu_{\text{SW}}$) is obtained only at $k_{\text{SW}} = 0$, while the matching is rapidly lost when k_{SW} increases, as can be seen in Figs. 2(c) and 2(f). This behavior can be explained taking into account the large dispersion of the lowest-frequency mode in DE geometry (see Fig. 8 in Appendix B). Therefore, at $\psi = 90°$ the measured velocity variation comes from a non-RMEC, and can be ascribed to the in-plane rotation of the sample magnetization towards the easy axis, when the intensity of the magnetic field is reduced.

Eventually, a constant decrease of the velocity variation is observed on decreasing the field amplitude when $\mathbf{B}_{\text{ext}}\|[100]$ [Fig. 3(b)] at both 833 and 119 MHz, since at $\psi = 45°$ the resonant condition $\nu_{\text{SAW}} = \nu_{\text{SW}}$ is far from being satisfied, as one can see in Figs. 2(b) and 2(e).

Finally, as can be seen in Fig. 4(b), a nonreciprocal SAW propagation is observed when $\mathbf{B}_{\text{ext}}\|[110]$, whereas the SAW nonreciprocity is not found when $\mathbf{B}_{\text{ext}}\|[1\bar{1}0]$ and $\mathbf{B}_{\text{ext}}\|[100]$. We recall that nonreciprocity means that SAW propagation (attenuation and velocity) depends on whether the acoustic wavevector is parallel or antiparallel to a given direction [26].

It is important to note that, in Ref. [8], SAW attenuation was found to change as a function of the magnetic field intensity only for $\psi = 0°$, while for $\psi = 45°$ and 90° the variation of SAW attenuation was negligible. Here, changes in the relative velocity variation were observed in all the investigate geometries and even off-resonance, suggesting that the relative velocity is much more sensitive to the magnetic configuration than to the acoustic attenuation.

In the next subsection we will describe the phenomenological model used to explain these experimental results.

B. Phenomenological magnetoelastic approach considering spin-wave dispersion

In this section we present the model used to interpret the evolution of the velocity variation as a function of both the in-plane direction and the intensity of the applied magnetic field. In a previous work Dreher *et al.* [12] developed a phenomenological approach to explain the dependence of the SAW attenuation as a function of the in-plane and out-of-plane angle between the applied magnetic field and the SAW propagation direction. In this approach the authors solved the Landau-Lifshitz-Gilbert (LLG) equation to obtain expressions for the magnetization dynamics and then took into account a purely longitudinal acoustic wave, instead of the more complicated Rayleigh wave, to establish the back action of the ferromagnetic resonance on the acoustic wave. Subsequently, both the longitudinal and the transverse terms of the Rayleigh wave were successfully taken into account in a semi-infinite medium approximation [23] and in a layered system by Hernández *et al.* [15,27] where the authors succeeded in describing the nonreciprocity of SAW attenuation. Previous studies by other authors have already shown the importance of dispersion of spin waves in attenuation analysis [14,15]. Here, we show that it is essential to take into account the dispersion of spin waves to explain the behavior of the velocity as a function of the applied field. Our starting point, in order to evaluate the relative SAW velocity change $\Delta V/V$ in epitaxial Fe thin films on a GaAs(001) substrate, is the following ansatz which we

adopt for Rayleigh waves [12,28]:

$$R_{\text{eff}}\Delta P = -2x_0\Delta\widetilde{k}_{\text{SAW}}P_{\text{ac}}^{\text{layer}}. \quad (1)$$

Here, ΔP is the maximum power that can be transmitted from the SAW to the magnetization dynamics (i.e., to SWs) and R_{eff} is an ad hoc parameter to compare calculations with experimental results. $P_{\text{ac}}^{\text{layer}}$ is the acoustic power carried by traveling SAWs in the layer (note that, contrary to Dreher *et al.* [12] who took into account the acoustic power of the wave, we consider here only the acoustic power in the layer); x_0, the propagation length of the magnetic device ($x_0 = 4$ mm in our case); and $\Delta\widetilde{k}_{\text{SAW}}$, a small perturbation of the wave number of the SAW. We assume a vector displacement $\mathbf{u}(\mathrm{X}) = \mathbf{u_0}e^{i(\widetilde{k}X-\omega t)}$ where $\widetilde{k}_{\text{SAW}} = k_{\text{SAW}} + iA$, and the amplitude A (m^{-1}) is linked to the attenuation Γ ($\text{dB}\,\text{m}^{-1}$) by the expression $\Gamma = (20/\ln 10)A$. Consequently, the complex quantity $\Delta\widetilde{k}_{\text{SAW}}$ is related to the variation of the SAW velocity (ΔV) and of the attenuation ($\Delta\Gamma$) by

$$\frac{\Delta V}{V} = -\frac{\text{Re}(\Delta\widetilde{k}_{\text{SAW}})}{k_{\text{SAW}}}, \quad \Delta\Gamma = \frac{20}{\ln 10}\,\text{Im}(\Delta\widetilde{k}_{\text{SAW}}). \quad (2)$$

The acoustic power can be derived from the approach given by Royer in Ref. [29]:

$$P_{\text{ac}}^{\text{layer}} = \frac{1}{2}\rho w v_R \omega^2 \int_0^d \left[|u_X|^2 + |u_Y|^2 + |u_Z|^2\right] dz, \quad (3)$$

where the u_i components are defined in the rotated frame ($X\|[110], Y\|[1\bar{1}0], Z\|[001]$), $w = 4$ mm is the acoustic beam width, v_R is the Rayleigh sound velocity in the [110] direction (see Table II), $\rho = 7851\ \text{kg}\,\text{m}^{-3}$ is the Fe mass density [30], and d is the magnetic film thickness (54 nm). In our case, $u_Y = 0$.

The electromagnetic power, ΔP, transmitted to the magnetic layer is calculated as follows [12,14,15]:

$$\Delta P = -\frac{\omega\mu_0 M_s}{2}\int_{V_0}\left[(h_\theta^*, h_\varphi^*)\bar{\chi}\begin{pmatrix}h_\theta\\ h_\varphi\end{pmatrix}\right] dV, \quad (4)$$

where θ and φ respectively denote the polar and azimuthal (with respect to the [110] direction) angle of the normalized magnetization vector, that is, $\mathbf{m} = \mathbf{M}/M_s$ where M_s is the saturation magnetization and V_0 is the Fe thin-film volume. $\bar{\chi}$ is the Polder susceptibility matrix [15] which describes the magnetic response of the ferromagnet to a small, time-varying magnetoelastic field (associated with the traveling SAW) whose out-of-plane (h_θ) and in-plane (h_φ) components are perpendicularly oriented with respect to the equilibrium magnetization $\mathbf{m}_0$. The explicit forms for h_θ, h_φ, and $\bar{\chi}$ in Eq. (4) can be obtained [15] in the framework of the LLG equation of motion for $\mathbf{m}$ [31]:

$$\partial_t\mathbf{m} = -\gamma\mathbf{m}\times\mu_0\mathbf{H}_{\text{eff}} + \alpha\mathbf{m}\times\partial_t\mathbf{m}, \quad (5)$$

where $\gamma > 0$ is the gyromagnetic ratio and α is a phenomenological damping parameter [31]. The time dependence of $\mathbf{m}$ is determined by the effective magnetic field $\mu_0\mathbf{H}_{\text{eff}} = -\nabla_{\mathbf{m}}f_{\text{tot}}$, where $f_{\text{tot}} = f + f_{\text{me}} + f_{\text{rot}}$ is the total free energy density (normalized to the saturation magnetization M_s), consisting of a purely magnetic contribution, f (reported in Appendix A), a magnetoelastic one, f_{me}, and a magnetorotation one, f_{rot}. For a cubic solid, f_{me} reads

$$f_{\text{me}} = B_1\left[\varepsilon_{xx}\left(m_x^2 - \frac{1}{3}\right) + \varepsilon_{yy}\left(m_y^2 - \frac{1}{3}\right) + \varepsilon_{zz}\left(m_z^2 - \frac{1}{3}\right)\right] + 2B_2(\varepsilon_{xy}m_xm_y + \varepsilon_{yz}m_ym_z + \varepsilon_{zx}m_zm_x), \quad (6)$$

where B_1 and B_2 are phenomenological magnetoelastic coupling constants [8], ε_{ij} are strain components ($i,j = x,y,z$) expressed in the standard cubic frame ($x\|[100], y\|[010], z\|[001]$), and m_i is the normalized magnetization component along i. mostly due to the shape anisotropy field directed along the z axis. Similarly to Xu *et al.* [17], we adopt the energy term reported by Tremolet [32, p. 78] for a tetragonal symmetry by considering that the magnetic shape anisotropy term is one order of magnitude larger that the magnetocrystalline out-of-plane uniaxial anisotropy, K_u (see Appendix B). As a consequence, the energy is given by

$$f_{\text{rot}} = \mu_0 M_S^2(\omega_{yz}m_ym_z + \omega_{xz}m_xm_z), \quad (7)$$

where the $\omega_{ij} = \frac{1}{2}[(\partial u_i/\partial x_j) - (\partial u_j/\partial x_i)]$ are the components of the rotation tensor [33].

Linearizing the LLG equation of motion, that is, considering small deviations, $\delta\theta$ and $\delta\varphi$, in the two directions perpendicular to the equilibrium magnetization $\mathbf{m}_0$, one obtains [15]

$$\begin{pmatrix}\delta\theta\\ \delta\varphi\end{pmatrix} = \bar{\chi}\begin{pmatrix}h_\theta\\ h_\varphi\end{pmatrix}. \quad (8)$$

For in-plane $\mathbf{m}_0$ [i.e., $\theta_0 = \pi/2$, and φ_0 given by Eq. (A6) in Appendix A], the effective field is obtained by calculating $-\nabla_{\mathbf{m}}(f_{\text{me}} + f_{\text{rot}})$. Thus, the out-of-plane and the in-plane components of the effective field read as follows [15,17]:

$$\mu_0 h_\theta = \frac{2B_2}{M_S}\cos\varphi_0\varepsilon_{XZ} - \mu_0 M_s\cos\varphi_0\omega_{XZ}, \quad (9a)$$

$$\mu_0 h_\varphi = \frac{2B_2}{M_S}\sin\varphi_0\cos\varphi_0\varepsilon_{XX}, \quad (9b)$$

where ε_{ij} ($i,j = X,Y,Z$) are the dynamical strain components defined in the rotated frame. It is very important

to report that we could have limited our approach to the in-plane field [Eq. (9b)] to give a satisfying description of the observed velocity field dependence. We decided to include the h_θ field in our calculations for completeness and accuracy and to estimate the expected nonreciprocity effects [34].

The Polder matrix $\bar{\chi}$ takes the form [15,35]

$$\bar{\chi} = \frac{\gamma\mu_0}{D}\begin{pmatrix} \gamma f_{\varphi\varphi}(\mathbf{k}_{SW}) - i\alpha\omega & -i\omega \\ i\omega & \gamma f_{\theta\theta}(\mathbf{k}_{SW}) - i\alpha\omega \end{pmatrix} \quad (10)$$

with

$$D = -(1+\alpha^2)\Big(\omega^2 - \omega_0^2(\mathbf{k}_{SW}) - i\omega\kappa\Big), \quad (11)$$

$$\omega_0^2(\mathbf{k}_{SW}) = \frac{\gamma^2}{\alpha^2+1} f_{\varphi\varphi}(\mathbf{k}_{SW}) f_{\theta\theta}(\mathbf{k}_{SW}) \quad (12)$$

$$\kappa = \gamma\frac{\alpha}{\alpha^2+1}\Big(f_{\varphi\varphi}(\mathbf{k}_{SW}) + f_{\theta\theta}(\mathbf{k}_{SW})\Big). \quad (13)$$

It is fundamental to notice the important ingredient of our approach: in our calculation of the Polder susceptibility, the spin-wave wavevector $\mathbf{k}_{SW}$ is explicitly taken into account through the dispersion relation of the lowest-frequency spin-wave mode, $\omega_0(\mathbf{k}_{SW})$, and the second derivatives of the purely magnetic free energy density, f.

Using dipole-exchange spin-wave theory [36] for a tangentially magnetized ferromagnetic film with thickness d, and neglecting the dipolar-induced hybridization between spin-wave modes in the low wavevector limit ($kd \ll 1$), the following approximate analytical expressions for $f_{\theta\theta}(\mathbf{k}_{SW})$ and $f_{\varphi\varphi}(\mathbf{k}_{SW})$ are obtained [37]:

$$\begin{aligned} f_{\theta\theta}(\mathbf{k}_{SW}) &= \mu_0 H\cos(\varphi_0-\psi) + \mu_0 M_s(1-P_{00}) \\ &\quad + \mu_0 H_1\frac{1}{4}[3-\cos(4\varphi_0)] - \mu_0 H_u \\ &\quad + \mu_0 H_{ex}(ka)^2, \end{aligned} \quad (14)$$

$$\begin{aligned} f_{\varphi\varphi}(\mathbf{k}_{SW}) &= \mu_0 H\cos(\varphi_0-\psi) + \mu_0 M_s P_{00}\sin^2\varphi_0 \\ &\quad - \mu_0 H_1\cos(4\varphi_0) + \mu_0 H_{ex}(ka)^2, \end{aligned} \quad (15)$$

where $\mu_0 H$ is the intensity of the external magnetic field; $\mu_0 H_1 = 2K_1/M_s$, $\mu_0 H_u = 2K_u/M_s$, and $\mu_0 H_{ex} = (2A_{ex})/(M_s a^2)$ denote effective magnetic field intensities, respectively associated with the cubic anisotropy energy density (K_1), the out-of-plane uniaxial anisotropy energy density (K_u), and the exchange energy density (A_{ex}/a^2, where a is the cubic cell length of Fe); $\mu_0 M_s$ is a magnetic dipolar field; and $P_{00} = 1 - [(1-e^{-kd})/kd]$ a dimensionless dipolar factor.

It is now worth noticing that, in the very low wavevector limit ($kd \ll 1$), analytical expressions [37] (not reported here) can be obtained also for the higher-frequency spin-wave modes (i.e., $\omega_n(\mathbf{k}_{SW})$ with $n = 1, 2, \ldots$), where the spin-wave wavevector $\mathbf{k}_{SW}$ can be approximately separated into a component ($\mathbf{k}$) tangential to the film plane, and the other ($k_{\perp,n} = n\pi/d$ with $n = 1, 2, \ldots$) perpendicular to the film plane. In the general case of finite in-plane wavevector, the calculation of the dipole-exchange spin-wave frequencies $\omega_n(\mathbf{k}_{SW})$ ($n = 0, 1, 2, \ldots$) instead requires the numerical diagonalization of a square matrix [36,37] because magnetic dipole-dipole interactions provide substantial hybridization between the SW modes for $kd \gtrsim 1$ [36,37].

In Appendix B (see Figs. 6–8) we compare BLS measurements of the SW frequencies and theoretical expressions for the three lowest SW modes ($n = 0, 1, 2$). We could thus obtain a quantitative evaluation of both the magnetic parameters and the thickness of our Fe film.

Finally, it is fundamental to remark that, on the basis of the SW dispersion relation measured by BLS for $k < 0.2\times10^7$ rad m^{-1} (very low wavevector; see Fig. 8 of Appendix B), the lowest-frequency mode corresponds to the mode $n = 0$. Therefore, in our calculation of the Polder susceptibility [Eq. (10)], only the lowest-frequency spin-wave mode, $\omega_0(\mathbf{k}_{SW})$, was taken into account.

C. Comparison with experimental results

Figures 3 and 4 report the comparison between the experimental and the calculated $\mathbf{B}_{ext}$-dependence of the velocity changes. Theoretical curves were obtained numerically using the approach described in the previous subsection.

As can be seen, very good agreement is found for different directions of the magnetic field (Fig. 3). In addition, for $\psi = 0°$ the theoretical calculations reproduce quite well the evolution of $\Delta V/V$ as a function of ν_{SAW} for all frequencies (Fig. 4), showing that the factor R_{eff} is proportional to the SAW frequency. In particular, it turns out that the best-fit proportionality factor is $R_{eff} = \nu_{SAW}/7050$ (ν_{SAW} in megahertz), permitting us to infer that this approach should be valid even at higher frequencies, provided that $\nu_{SAW} < 7050$ MHz.

It is important to report that similar calculations performed in the uniform ($k_{SAW} = 0$) approximation give very similar trends for the $\psi = 0°$ and $\psi = 90°$ geometries, with sharp variations at B_r. However, experimentally these two configurations do not show the same trend. Consequently, the k-dispersion has a strong impact on magnetic-field-induced velocity changes.

Note that the theoretical curves calculated for $\mathbf{B}_{ext}\|[110]$ exhibit a much sharper variation than the experimental ones. We ascribe this observation to the mosaicity of the sample [the FWHM of the (002) planes is approximately 0.3°, as measured by x-ray diffraction], which is responsible for a spreading of the resonant frequencies at a given B_{ext} [8].

In the previous section we anticipated that a satisfying description of the observed velocity change field dependence is obtained by taking $h_\theta = 0$ in Eq. (9a). This is described in Appendix C where good agreement between experimental results and a fully longitudinal wave approach is found for $R_{\text{eff}} = \nu_{\text{SAW}}/24\,000$ (ν_{SAW} in megahertz). This approach is much simpler, as already shown for SAW attenuation measurements in Ref. [12]. Interestingly, the h_θ component is crucial to understanding the origin of nonreciprocal phenomena. Indeed, following Xu *et al.* [17], we find that the magnetorotational coupling, that is, the second term of the h_θ field in Eq. (9a), is the source of the observed nonreciprocity in Fig. 4(b). Indeed, when this term is not taken into account a nearly perfect reciprocity is recovered (not shown).

Finally, in order to evidence the impact of RMEC and of magnetization dynamics on the velocity variation, we calculate $\Delta V/V$ on changing the Gilbert damping, α (Fig. 5). One can see that the sharp velocity change observed around $B_r \approx 58$ mT for $\psi = 0^\circ$ broadens when the dynamics is turned off by an artificially high value of α. We notice that the overdamped velocity change obtained with $\alpha = 2$ well describes the experimental results for $\mathbf{B}_{\text{ext}} \perp \mathbf{k}_{\text{SAW}}$ ($\psi = 90^\circ$). This permits us to conclude that the sharp-shape velocity change observed for $\psi = 0^\circ$ is a genuine fingerprint of the resonant SAW-induced magnetization precession, and that the smoother $\mathbf{B}_{\text{ext}}$ dependence observed in the case $\psi = 90^\circ$ is the nonresonant expected trend.

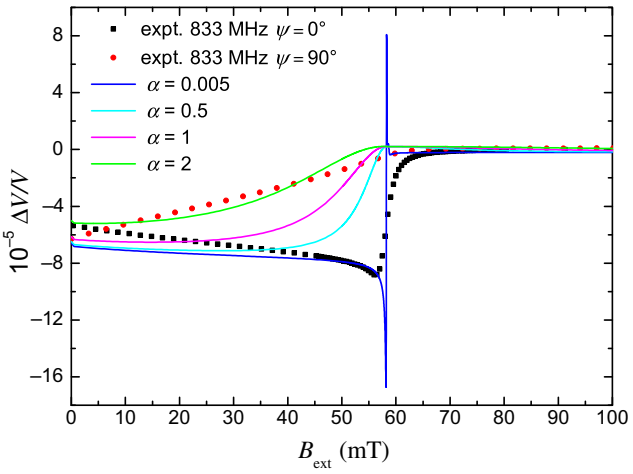

FIG. 5. Relative variation of the SAW velocity V measured versus decreasing amplitude of the external field B_{ext} at $\nu_{\text{SAW}} =$ 833 MHz at $\psi = 0^\circ$ and $\psi = 90^\circ$ as represented in Figs. 3(a) and 3(c). The solid lines correspond to the simulation results using the model in Sec. III B for different values of the Gilbert parameter at $\psi = 0^\circ$. The α parameter was exaggerated in order to let the resonant dynamical effects fade out.

D. Fully magnetoelastic approach for $k_{\text{SAW}} = 0$

In order to corroborate our phenomenological approach based on Eq. (1), we developed an alternative fully elastic approach based on SAW propagation in a layered structure. Here, we consider a thin Fe film epitaxied on top of a GaAs substrate. Both systems present a cubic structure with the same orientation. Magnetism is considered by introducing additional magnetic terms in the stress versus strain relations. In the case of in-plane equilibrium magnetization ($\theta_0 = \pi/2$ and $\varphi = \varphi_0$), we have [38]

$$\begin{aligned}
\sigma_{XX} &= \widehat{C}'_{11}\varepsilon_{XX} + \widehat{C}'_{13}\varepsilon_{ZZ} + B_2\cos(2\varphi_0)\delta\varphi,\\
\sigma_{YY} &= \widehat{C}'_{12}\varepsilon_{XX} + \widehat{C}'_{23}\varepsilon_{ZZ} - B_2\cos(2\varphi_0)\delta\varphi,\\
\sigma_{ZZ} &= \widehat{C}'_{13}\varepsilon_{XX} + \widehat{C}'_{33}\varepsilon_{ZZ},\\
\sigma_{XY} &= B_1\sin(2\varphi_0)\delta\varphi,\\
\sigma_{XZ} &= 2\widehat{C}'_{55}\varepsilon_{XZ} - B_2\sin(\varphi_0 + \pi/4)\delta\theta,\\
\sigma_{YZ} &= -B_2\sin(\varphi_0 - \pi/4)\delta\theta,
\end{aligned} \tag{16}$$

where B_1 and B_2 are magnetoelastic constants, defined in the standard cubic frame, that is, axis parallel to [100], [010], [001] directions [see Eq. (6)]. σ_{ij}, ε_{ij}, and $\widehat{C}'_{ij}$ are the stress, strain, and elastic constants, in the layer, written in a rotated frame, that is, axis parallel to [110], [$\bar{1}$10], [001] directions (elastic constant values in Appendix D).

In both layer and substrate, we assume that the SAW is a linear combination of partial waves. This is the standard procedure in the derivation of the surface waves in purely elastic layered structure. Partial waves are given by

$$\begin{aligned}
u_X &= U\exp(-\xi Z)\exp i(kX - \omega t),\\
u_Y &= 0,\\
u_Z &= W\exp(-\xi Z)\exp i(kX - \omega t)
\end{aligned} \tag{17}$$

in the substrate, and

$$\begin{aligned}
\widehat{u}_X &= \widehat{U}\exp(-\widehat{\xi}Z)\exp i(kX - \omega t),\\
\widehat{u}_Y &= 0,\\
\widehat{u}_Z &= \widehat{W}\exp(-\widehat{\xi}Z)\exp i(kX - \omega t),\\
\delta\varphi &= \Phi\exp(-\widehat{\xi}Z)\exp i(kX - \omega t),\\
\delta\theta &= \Theta\exp(-\widehat{\xi}Z)\exp i(kX - \omega t)
\end{aligned} \tag{18}$$

in the layer, where u_i and $\widehat{u}_i$ are the displacement fields in the rotated frame, and in the layer and substrate, respectively. X and Z are the coordinates along the propagation axis [110] and along the out-of-plane axis [001], respectively.

We then look for a solution satisfying both the equations of motion and the elastic boundary conditions, at the

surface and the interface. This calculation is quite tedious but it makes the bridge between theory of elasticity and magnetization dynamics. Since our aim is to corroborate the intensity of the R_{eff}-factor and understand its origin, we simplify our approach (i) by neglecting the magnetic boundary conditions as in Refs. [12] and [15], (ii) by solving the LLG equations in a uniform mode approach, and (iii) by neglecting the magnetorotational term. This approximation is valid for $\nu_{\text{SAW}} = 119$ MHz (corresponding to $k_{\text{SAW}} = 0.262\ \mu\text{m}^{-1}$) and $\psi = 0^\circ$ for which the magnetic dynamic parameters $f_{\theta\theta}$ and $f_{\varphi\varphi}$ in the uniform mode approximation are very close to the exact values (not shown here). We also assume that the damping term α is zero. We suppose that nonreciprocity is a small effect that can be neglected for this elastic approach. Using this approach, we calculate $\Delta k_{\text{SAW}}/k_{\text{SAW}}$ and $\Delta P/P_{\text{ac}}^{\text{layer}}$ and obtain $R_{\text{eff}} = \nu_{\text{SAW}}/9434$. We consider that the values of R_{eff} determined by the two models are in good agreement considering the accuracy of the models.

This result is important since it demonstrates that the intensity of the MEC interaction is fully described by a standard model based on elasticity, describing SAW propagation in a layered elastic structure; that is, no hidden or more complicate interactions have to be considered. Moreover, we show that the much simpler phenomenological magnetoelastic approach based on Eq. (1) and presented in Sec. III B can be safely adopted to describe the magnetoelastic coupling in Fe thin films, once $R_{\text{eff}} \approx \nu_{\text{SAW}}/7050$.

IV. CONCLUSIONS

In this work we have investigated the dependence of the SAW velocity variation as a function of the in-plane direction of the external applied magnetic field $\mathbf{B}_{\text{ext}}$ in a Fe thin film grown on a GaAs substrate. In order to explain the experimental results we have taken a phenomenological approach, where the SW dispersion has been explicitly included by solving the LLG equation. We have demonstrated that $\Delta V/V$ not only depends on the orientation between $\mathbf{B}_{\text{ext}}$ and $\mathbf{k}_{\text{SAW}}$, but also is more sensitive to the SW dispersion than the SAW attenuation. Moreover, we have introduced a proportionality parameter R_{eff} that describes the intensity of the magnetoacoustic interaction of SAWs traveling in a multilayer, that is, a magnetic thin film over a piezoelectric substrate. The parameter R_{eff} is observed to be proportional to the SAW frequency. Remarkably, the best-fitted value of this parameter $R_{\text{eff}} = \nu_{\text{SAW}}/7050$ is found to describe well the velocity change for all the probed frequencies and magnetic field directions. Despite the approximation involved, this approach gives a very good description of the SAW-SW interaction in the $(\mathbf{k}, \omega)$ space. In this context, our findings give a comprehensive and quantitative picture of the magnetic field control of the SAW-SW interaction. Beyond magnonic applications, our experimental results and theoretical models allow us to envisage alternative functionalities even for the more mature SAW technology. Here, we put forward the idea of a tunable SAW filter where the SAW phase and/or the resonance frequency can be controlled by a judicious and fine orientation of a permanent magnet. For instance, microelectromechanical systems could be exploited to finely control the orientation of the magnetic field with respect to the propagation direction of the SAW, in order to modify the SWs properties and control the dynamic magnetoelastic coupling. Our velocity changes are still moderate (of the order of 10^{-5}) but comparable with phase tunable SAW device on $LiNbO_3$ substrate [39]. However by increasing the film thickness and by adopting materials with enhanced magnetoelastic and piezoelectric couplings (e.g., $TbCo_2$/FeCo thin film on $LiNbO_3$ in Ref. [5]) the frequency shift can be increased by several orders of magnitude.

ACKNOWLEDGMENTS

The authors acknowledge C. Gourdon and L. Thevenard for fruitful discussions and careful reading of the manuscript of this paper. They acknowledge the staff of the MPBT (Physical Properties Low Temperature) platform of Sorbonne University for their support, as well as L. Becerra and M. Rosticher for optical and electronic lithography and A. Anane for dry etching. The authors acknowledge support from the Agence National de la Recherche Française Grant No. ANR-22-CE24-0015 SACOUMAD and from the European Union within the HORIZON-CL4-2021-DIGITAL-EMERGING-01 Grant No. 101070536 MandMEMS.

APPENDIX A

The purely magnetic free energy density, f, normalized to the saturation magnetization (M_s), can be expressed as the sum of four terms,

$$f = f_Z + f_1 + f_u + f_d, \tag{A1}$$

where the Zeeman (f_Z), cubic (f_1), uniaxial out-of-plane (f_u), and dipolar (f_d) contributions are respectively given by

$$f_Z = -\mu_0 H\Big[\sin\theta \sin\theta_H \cos(\varphi - \psi) + \cos\theta \cos\theta_H\Big], \tag{A2}$$

$$f_1 = \frac{1}{2}\mu_0 H_1\Big[\sin^2\theta \cos^2\theta + \sin^4\theta \frac{1+\cos(4\varphi)}{8}\Big], \tag{A3}$$

$$f_u = \frac{1}{2}\mu_0 H_u \sin^2\theta, \tag{A4}$$

$$f_d = -\frac{1}{2}\mu_0 \mathbf{h_d}\cdot\mathbf{m}, \tag{A5}$$

in which $\mu_0 H_1 = 2K_1/M_s$ and $\mu_0 H_u = 2K_u/M_s$ are effective magnetic fields associated with the cubic anisotropy constant (K_1) and the uniaxial out-of-plane anisotropy constant (K_u), respectively. The dipolar field, $\mathbf{h_d}$, in general does not take a closed form [36,40].

The equilibrium direction of the magnetization is obtained by imposing the vanishing of the first derivatives of the purely magnetic free energy density, f , with respect to polar and azimuthal angle θ and φ, respectively ($f_\theta = 0$ and $f_\varphi = 0$). When the external magnetic field is applied in plane ($\theta_H = \pi/2$), we assume the easy-plane dipolar anisotropy energy of the film to be stronger than the out-of-plane uniaxial anisotropy, so that the first condition ($f_\theta = 0$) is fulfilled by $\theta_0 = \pi/2$, meaning that also the equilibrium magnetization lies in the film plane. The second condition ($f_\varphi = 0$) provides φ_0, that is, the equilibrium azimuthal angle of the in-plane magnetization with respect to the [110] axis, as the solution of the equation

$$H \sin(\varphi_0 - \psi) - \frac{1}{4} H_1 \sin(4\varphi_0) = 0. \qquad \text{(A6)}$$

In the absence of the external field ($H = 0$), one has that for $K_1 > 0$ the equilibrium magnetization is parallel to [100] (i.e., $\varphi_0 = \pi/4$; see Fig. 1). If the external field is applied parallel to the hard axis, $\mathbf{H}\|[110]$ (i.e., $\psi = 0$), the equilibrium angle φ_0 gradually decreases from $\pi/4$ to 0, when H is increased from 0 to H_1. Finally, for $H > H_1$ the equilibrium magnetization remains parallel to the external field (i.e., $\varphi_0 = \psi = 0$).

APPENDIX B

BLS and BB-FMR measurements were performed in order to quantitatively evaluate the magnetic parameters of the Fe film.

BLS measurements were carried out in the backscattering geometry, focusing about 200 mW of monochromatic light (wavelength $\lambda = 532$ nm) onto the sample surface. The scattered light was frequency-analyzed by a Sandercock-type 3+3-pass tandem Fabry-Perot interferometer. BB-FMR measurements were performed using a vector network analyzer which measures the S_{ij} parameters as a function of the frequencies at a fixed external magnetic field from 850 to 50 mT. The thin-film sample is positioned at the center of a coplanar waveguide with a center strip 300 μm wide. Each S_{12} parameter was normalized by the S_{12} parameter at a reference field of 150 mT.

The experimental data were analyzed by using a theory of dipole-exchange spin waves, propagating in plane in a tangentially magnetized thin ferromagnetic film, presented in detail in previous works [36,37].

The best agreement with the experimental data was obtained using the following magnetic parameters: gyromagnetic factor [41] $\gamma/2\pi = 29.4$ GHz T^{-1}, saturation magnetization $M_s = 1.7 \times 10^6$ A m^{-1}, exchange coupling $A_{ex} = 2.0 \times 10^{-11}$ J m^{-1}, cubic anisotropy $K_1 = 4.96 \times 10^4$ J m^{-3}, and out-of-plane uniaxial anisotropy $K_u = 1.0 \times 10^5$ J m^{-3}. In addition, the fit of BLS experimental data provided an accurate estimate not only of the magnetic parameters, but also of the film thickness, $d = 54$ nm (a slightly smaller value than in Ref. [8]).

Figure 6 shows the dependence of the SW frequency as a function of the in-plane angle ψ between the in-plane applied magnetic field and the [110] Fe direction, measured by BLS at $\mathbf{k} = 0$ rad m^{-1} for $B_{ext} = 200$ mT. As can be seen, the sample exhibits the expected bulk Fe cubic anisotropy, whose easy and hard axes are along the [100] and [110] directions, respectively. The lowest-frequency mode corresponds to the uniform mode ($n = 0$), while the second and the third mode can be identified as the first and second perpendicular standing spin-wave mode characterized by $n = 1$ and $n = 2$ nodes across the film thickness.

In Fig. 7, we report the SW frequencies measured by means of BLS and BB FMR as a function of the magnitude of an external magnetic field, applied along the in-plane [110] hard axis. Note that the mode observed in BB-FMR measurements is in quite good agreement with the lowest-frequency mode measured by BLS. All the modes are characterized by a nonmonotonic behavior with a local minimum at about 58 mT. This is a typical hard-axis behavior, and indicates a reorientation of the magnetization towards the nearest easy axis when the intensity of the applied field is reduced from saturation. Note that the

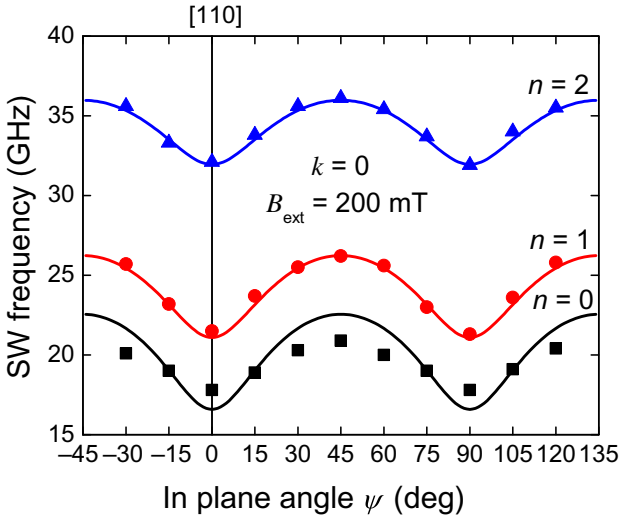

FIG. 6. Angular dependence of the three lowest-frequency SW modes ($n = 0, 1, 2$), measured (symbols) by BLS and calculated (lines) using dipole-exchange SW theory [37] for a Fe film with thickness $d = 54$ nm, at zero in-plane wavevector ($k = 0$) and fixed intensity ($B_{ext} = 200$ mT) of the in-plane applied magnetic field. ψ is the angle formed by $\mathbf{B}_{ext}$ with respect to [110].

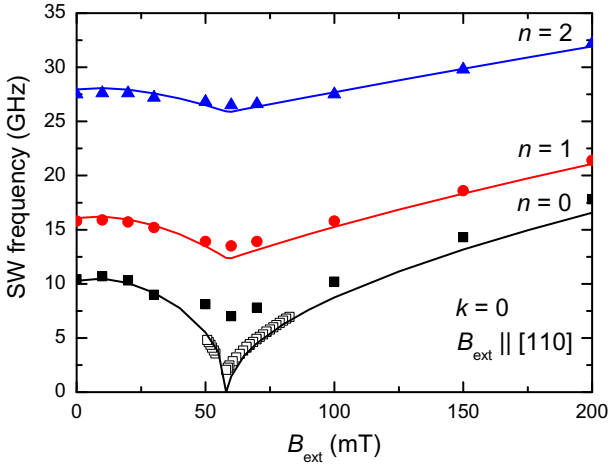

FIG. 7. Dependence of the three lowest-frequency SW modes ($n = 0, 1, 2$) as a function of the external field magnitude, measured by BLS (filled symbols) and BB FMR (open symbol) at zero in-plane wavevector ($k = 0$) and calculated (lines) using dipole-exchange SW theory [37] for a Fe film with thickness $d = 54$ nm. The magnetic field is applied in plane along the hard [110] axis.

frequency of the lowest-frequency mode is observed to reach an almost zero value in the BB-FMR measurements around $B_r = 58$ mT, while it retains a frequency of about 7 GHz in the BLS ones. This difference can be attributed to a small misalignment of the applied field with respect to the hard axis [8] in the BLS measurements.

The SW dispersion measured by BLS is shown in Fig. 8. Measurements were performed in the DE configuration applying a magnetic field of $B_{ext} = 200$ mT along the [110] hard axis, and sweeping the in-plane wavevector along the

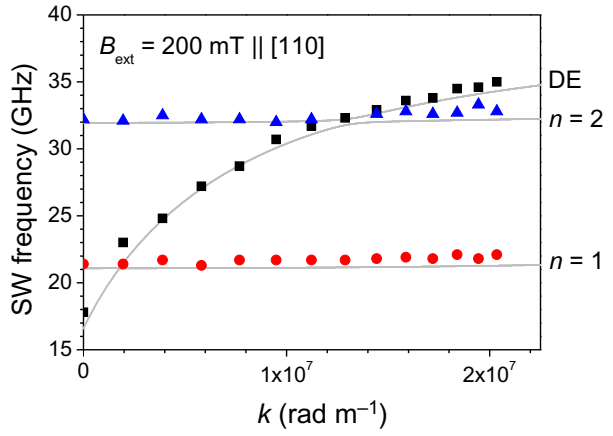

FIG. 8. SW dispersion measured (symbols) by BLS and calculated (lines) using dipole-exchange SW theory [37] for a Fe film with thickness $d = 54$ nm. A magnetic field of fixed intensity ($B_{ext} = 200$ mT) is applied in plane along the hard [110] axis.

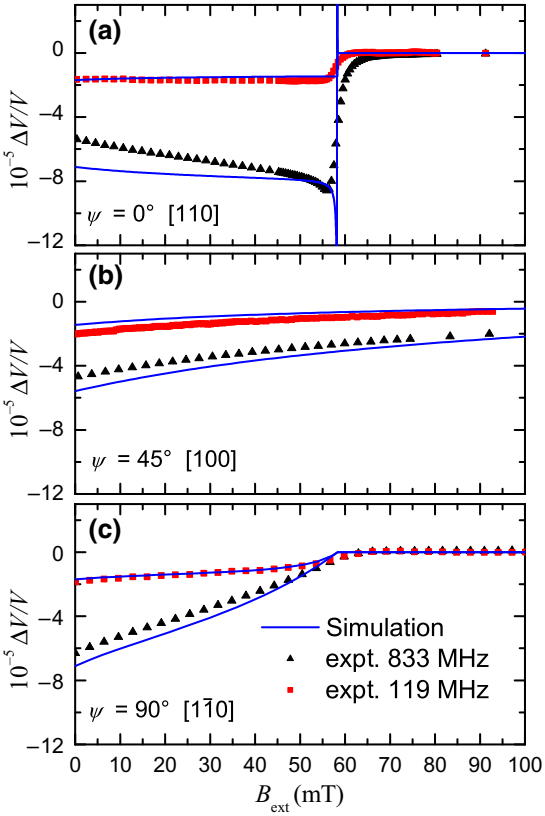

FIG. 9. The same as Fig. 3. Here, calculations consider purely longitudinal waves and the correct SWs dispersion with a Gilbert constant $\alpha = 0.005$.

perpendicular direction. Due to the conservation of the in-plane momentum in the scattering process, the wavevector magnitude k is linked to the incidence angle of light θ by the relation $k = (4\pi/\lambda)\sin\theta$. Note that the product of film thickness ($d = 54$ nm) and wavevector range ($k < 2 \times 10^7$ rad m^{-1}) is not negligible; therefore, the spin-wave frequencies in Fig. 8 were calculated taking into account the hybridization between the modes [37]. As can be seen, the first ($n = 1$) and second ($n = 2$) perpendicular standing spin-wave modes are characterized by a dispersionless behavior. In contrast, the lowest-frequency mode ($n = 0$) exhibits a positive dispersion typical of the DE mode. In fact, in the DE geometry for wavevectors different from zero, the uniform mode becomes the DE mode, which is mainly localized at the film surfaces.

TABLE I. Mass density (kg m^{-3}) and elastic constants (GPa) of Fe [30] and GaAs [42].

		Standard			Rotated		
	ρ	C_{11}	C_{12}	C_{44}	C'_{11}	C'_{12}	C'_{44}
Fe	7851	230.4	134.1	115.9	298.15	66.35	115.9
GaAs	5317	118.4	53.7	59.1	145.15	26.95	59.1

TABLE II. Elastic parameters used in calculations based on Eqs. (1), (3) and (4). Angle brackets stand for the mean value over the thickness of the iron layer. The values are normalized by imposing a total acoustic power of 1 W. Calculations are not affected by this arbitrary normalization. P_{ac}^{total} is the total acoustic power carried by the surface wave. P_{ac}^{layer} is the acoustic power carried by the surface wave only in the iron layer.

Frequency (MHz)	119	357	595	833
v_{SAW} (m s^{-1})	2856.24	2862.12	2866.20	2868.78
$\langle\lvert\varepsilon_{XZ}\rvert^2\rangle$	1.60×10^{-11}	4.11×10^{-10}	1.77×10^{-9}	4.54×10^{-9}
$\langle\lvert\varepsilon_{XX}\rvert^2\rangle$	5.61×10^{-7}	1.52×10^{-6}	2.31×10^{-6}	2.97×10^{-6}
$\langle\varepsilon_{XX} \times \overline{\varepsilon_{XZ}}\rangle$	$-2.57 \times 10^{-9} \times i$	$-2.14 \times 10^{-8} \times i$	$-5.45 \times 10^{-8} \times i$	$-9.82 \times 10^{-8} \times i$
$\langle\lvert\omega_{XZ}\rvert^2\rangle$	1.06×10^{-6}	3.20×10^{-6}	5.37×10^{-6}	7.58×10^{-6}
$\langle\varepsilon_{XZ} \times \overline{\omega_{XZ}}\rangle$	-3.55×10^{-9}	-3.14×10^{-8}	-8.44×10^{-8}	-1.61×10^{-7}
$\langle\varepsilon_{XX} \times \overline{\omega_{XZ}}\rangle$	$7.71 \times 10^{-7} \times i$	$2.21 \times 10^{-6} \times i$	$3.52 \times 10^{-6} \times i$	$4.73 \times 10^{-6} \times i$
$\langle\lvert u_X\rvert^2\rangle$ (m^2)	8.18×10^{-18}	2.48×10^{-18}	1.36×10^{-18}	8.90×10^{-19}
$\langle\lvert u_Z\rvert^2\rangle$ (m^2)	1.56×10^{-17}	5.30×10^{-18}	3.25×10^{-18}	2.37×10^{-18}
$\langle\lvert u_X\rvert\rangle$ (m)	2.86×10^{-9}	1.57×10^{-9}	1.16×10^{-9}	9.42×10^{-10}
$\langle\lvert u_Z\rvert\rangle$ (m)	3.94×10^{-9}	2.30×10^{-9}	1.80×10^{-9}	1.54×10^{-9}
$\langle\lvert\varepsilon_{XX}\rvert\rangle$	7.48×10^{-4}	1.23×10^{-3}	1.52×10^{-3}	1.72×10^{-3}
$\langle\lvert\varepsilon_{XZ}\rvert\rangle$	3.45×10^{-6}	1.75×10^{-5}	3.65×10^{-5}	5.85×10^{-5}
$\langle\lvert\omega_{XZ}\rvert\rangle$	1.03×10^{-3}	1.79×10^{-3}	2.32×10^{-3}	2.75×10^{-3}
P_{ac}^{layer} (W)	8.04×10^{-3}	2.38×10^{-2}	3.91×10^{-2}	5.44×10^{-2}
P_{ac}^{total} (W)	1	1	1	1

APPENDIX C

As already pointed out by Dreher *et al.* [12], a much simpler description of the magnetic field dependence of SAW propagation can be obtained by considering longitudinal waves and by neglecting both strain and rotation terms, that is, $h_\theta = 0$ in Eq. (9a). This is shown in Fig. 9 where good agreement between experimental results and this simplified approach is found for $R_{eff} = v_{SAW}/24\ 000$ (v_{SAW} in megahertz). A comparison with Fig. 3 attests that the longitudinal waves approach is sufficient to describe the observed velocity change.

APPENDIX D

In Table I the elastic constants of Fe and GaAs are reported in the standard and rotated frame.

Table II displays characteristics of the surface acoustic waves. Some values are needed to carry on calculations based on Eqs. (1), (3), and (4).

In Table III the magnetic parameters of Fe used in previous calculations are reported.

TABLE III. Magnetic parameters of Fe.

Gyromagnetic factor	$\gamma = 1.847 \times 10^{11}$ Hz T^{-1}
Saturation magnetization	$M_S = 1.7 \times 10^6$ A m^{-1}
Exchange coupling	$A_{ex} = 2.0 \times 10^{-11}$ J m^{-1}
Cubic anisotropy	$K_1 = 4.96 \times 10^4$ J m^{-3}
Out-of-plane uniaxial anisotropy	$K_u = 1.0 \times 10^5$ J m^{-3}
Magnetoelastic constant	$B_2 = -7 \times 10^6$ J m^{-3}

[1] C. Kittel, Interaction of spin waves and ultrasonic waves in ferromagnetic crystals, Phys. Rev. **110**, 836 (1958).

[2] A. V. Chumak, V. I. Vasyuchka, A. A. Serga, and B. Hillebrands, Magnon spintronics, Nat. Phys. **11**, 453 (2015).

[3] A. Barman, *et al.*, The 2021 magnonics roadmap, J. Phys.: Condens. Matter **33**, 413001 (2021).

[4] R. Li, G. Li, W. C. Hong, P. I. Reyes, K. Tang, K. Yang, S. Y. Wang, H. Ye, Y. Li, L. Zhang, K. Kisslinger, and Y. Lu, Tunable surface acoustic wave device using semiconducting MgZnO and piezoelectric NiZnO dual-layer structure on glass, Smart Mater. Struct. **27**, 085025 (2018).

[5] H. Zhou, A. Talbi, N. Tiercelin, and O. Bou Matar, Multilayer magnetostrictive structure based surface acoustic wave devices, Appl. Phys. Lett. **104**, 114101 (2014).

[6] M. Weiler, L. Dreher, C. Heeg, H. Huebl, R. Gross, M. S. Brandt, and S. T. Goennenwein, Elastically Driven Ferromagnetic Resonance in Nickel Thin Films, Phys. Rev. Lett. **106**, 117601 (2011).

[7] P. Kuszewski, J.-Y. Duquesne, L. Becerra, A. Lemaître, S. Vincent, S. Majrab, F. Margaillan, C. Gourdon, and L. Thevenard, Optical Probing of Rayleigh Wave Driven Magnetoacoustic Resonance, Phys. Rev. Appl. **10**, 34036 (2018).

[8] J.-Y. Duquesne, P. Rovillain, C. Hepburn, M. Eddrief, P. Atkinson, A. Anane, R. Ranchal, and M. Marangolo, Surface-Acoustic-Wave Induced Ferromagnetic Resonance in Fe Thin Films and Magnetic Field Sensing, Phys. Rev. Appl. **12**, 024042 (2019).

[9] L. Thevenard, I. S. Camara, S. Majrab, M. Bernard, P. Rovillain, A. Lemaître, C. Gourdon, and J.-Y. Duquesne, Precessional magnetization switching by a surface acoustic wave, Phys. Rev. B **93**, 134430 (2016).

[10] M. Weiler, H. Huebl, F. S. Goerg, F. D. Czeschka, R. Gross, and S. T. B. Goennenwein, Spin Pumping with Coherent Elastic Waves, Phys. Rev. Lett. **108**, 176601 (2012).

[11] P. Rovillain, R. Cardoso De Oliveira, M. Marangolo, and J.-Y. Duquesne, Nonsymmetric spin pumping in a multiferroic heterostructure, Phys. Rev. B **102**, 184409 (2020).

[12] L. Dreher, M. Weiler, M. Pernpeintner, H. Huebl, R. Gross, M. S. Brandt, and S. T. B. Goennenwein, Surface acoustic wave driven ferromagnetic resonance in nickel thin films: Theory and experiment, Phys. Rev. B **86**, 134415 (2012).

[13] G. Carlotti and G. Gubbiotti, Brillouin scattering and magnetic excitations in layered structures, Riv. Nuovo Cim. **22**, 1 (1999).

[14] P. G. Gowtham, T. Moriyama, D. C. Ralph, and R. A. Buhrman, Traveling surface spin-wave resonance spectroscopy using surface acoustic waves, J. Appl. Phys. **118**, 233910 (2015).

[15] A. Hernández-Mínguez, F. Macià, J. M. Hernàndez, J. Herfort, and P. V. Santos, Large Nonreciprocal Propagation of Surface Acoustic Waves in Epitaxial Ferromagnetic/Semiconductor Hybrid Structures, Phys. Rev. Appl. **13**, 44018 (2020).

[16] N. K. Babu, A. Trzaskowska, P. Graczyk, G. Centała, S. Mieszczak, H. Głowiński, M. Zdunek, S. Mielcarek, and J. W. Kłos, The interaction between surface acoustic waves and spin waves: The role of anisotropy and spatial profiles of the modes, Nano Lett. **21**, 946 (2021).

[17] M. Xu, K. Yamamoto, J. Puebla, K. Baumgaertl, B. Rana, K. Miura, H. Takahashi, D. Grundler, S. Maekawa, and Y. Otani, Nonreciprocal surface acoustic wave propagation via magneto-rotation coupling, Sci. Adv. **6**, eabb1724 (2020).

[18] R. Verba, I. Lisenkov, I. Krivorotov, V. Tiberkevich, and A. Slavin, Nonreciprocal Surface Acoustic Waves in Multilayers with Magnetoelastic and Interfacial Dzyaloshinskii-Moriya Interactions, Phys. Rev. Appl. **9**, 064014 (2018).

[19] M. Küß, M. Heigl, L. Flacke, A. Hefele, A. Hörner, M. Weiler, M. Albrecht, and A. Wixforth, Symmetry of the Magnetoelastic Interaction of Rayleigh and Shear Horizontal Magnetoacoustic Waves in Nickel Thin Films on $LiTaO_3$, Phys. Rev. Appl. **15**, 34046 (2021).

[20] The thickness of 67 nm reported in [8] was the nominal one. After examination and comparison with BLS data (see in particular Fig. 6 in Appendix B), the actual thickness was found to be 54 nm.

[21] M. Marangolo, F. Gustavsson, G. M. Guichar, M. Eddrief, J. Varalda, V. H. Etgens, M. Rivoire, F. Gendron, H. Magnan, D. H. Mosca, and J. M. George, Structural and magnetic anisotropies of Fe/ZnSe(001) thin films, Phys. Rev. B **70**, 134404 (2004).

[22] F. J. Schülein, E. Zallo, P. Atkinson, O. G. Schmidt, R. Trotta, A. Rastelli, A. Wixforth, and H. J. Krenner, Fourier synthesis of radiofrequency nanomechanical pulses with different shapes, Nat. Nanotechnol. **10**, 512 (2015).

[23] L. Thevenard, C. Gourdon, J. Y. Prieur, H. J. Von Bardeleben, S. Vincent, L. Becerra, L. Largeau, and J.-Y. Duquesne, Surface-acoustic-wave-driven ferromagnetic resonance in (Ga, Mn)(As, P) epilayers, Phys. Rev. B **90**, 94401 (2014).

[24] All the results are shown with a reference field at saturation to be sure of the magnetic state. At high fields, the velocity values differ, depending on the frequency and the magnetization vector direction. Consequently, at zero field the phase shifts for all measurements do not overlap.

[25] It turns out that the lowest-frequency mode corresponds to the uniform mode for $k_{SW} = 0$ and to the Damon-Eshbach for k_{SW} different from zero.

[26] R. Sasaki, Y. Nii, Y. Iguchi, and Y. Onose, Nonreciprocal propagation of surface acoustic wave in $Ni/LiNbO_3$, Phys. Rev. B Rapid Commun. **95**, 20407 (2017).

[27] P. Kuszewski, I. S. Camara, N. Biarrotte, L. Becerra, J. von Bardeleben, W. S. Torres, A. Lemaître, C. Gourdon, J.-Y. Duquesne, and L. Thevenard, Resonant magneto-acoustic switching: influence of rayleigh wave frequency and wavevector, J. Phys.: Condens. Matter **30**, 244003 (2018).

[28] This equation is correlated with the quasiexact model in Sec. III D via the evaluation of a proportionality factor R.

[29] D. Royer, E. Dieulesaint, and D. P. Morgan, *Elastic Waves in Solids* (Springer, Berlin, 2000).

[30] J. J. Adams, D. S. Agosta, R. G. Leisure, and H. Ledbetter, Elastic constants of monocrystal iron from 3 to 500 K, J. Appl. Phys. **100**, 113530 (2006).

[31] T. G. Gilbert, A phenomenological theory of damping in ferromagnetic materials, IEEE Trans. Magn. **40**, 3443 (2004).

[32] E. du Tremolet de Lacheisserie, *Magnetostriction Theory and Applications of Magnetoelasticity* (CRC Press, Boca Raton, FL, 1993).

[33] The cubic symmetry for the magnetoelastic energy of Eq. (6) still holds despite the overall tetragonal symmetry as shown in Barturen *et al.* [43].

[34] ω_{XZ} is much smaller than ε_{XZ} at the surface (see Table II). At odds with Refs. [15,26], we consider that the two terms of Eq. (9a) must be retained, as shown by [17].

[35] The matrix was not inverted and the saturated magnetization M_s was missing.

[36] B. A. Kalinikos and A. N. Slavin, Theory of dipole-exchange spin wave spectrum for ferromagnetic films with mixed exchange boundary conditions, J. Phys. C **19**, 7013 (1986).

[37] S. Tacchi, R. Silvani, G. Carlotti, M. Marangolo, M. Eddrief, A. Rettori, and M. G. Pini, Strongly hybridized dipole-exchange spin waves in thin Fe-N ferromagnetic films, Phys. Rev. B **100**, 104406 (2019).

[38] C. Hepburn, Dynamic interplay between the magnetization and surface acoustic waves in magnetostrictive $Fe_{(1-x)}Ga_{(x)}$ thin films. Thesis, Université Pierre et Marie Curie—Paris VI (2017).

[39] K. S. Kao, C. J. Chung, Y. C. Chen, C. C. Cheng, Phase tunable SAW device on $LiNbO_3$ substrate, Ferroelectrics **304**, 139 (2004).

[40] For zero wavevector the dipolar free energy takes the simple expression $f_d = -\frac{1}{2}\mu_0 M_s \sin^2\theta$ [15,44].

[41] A. Stollo, M. Madami, S. Tacchi, G. Carlotti, M. Marangolo, M. Eddrief, and V. H. Etgens, Brillouin light scattering study of magnetic anisotropy in epitaxial Fe/ZnSe(001) ultrathin films, Surf. Sci. **601**, 4316 (2007).

[42] R. I. Cottam and G. A. Saunders, The elastic constants of GaAs from 2 K to 320 K, J. Phys. C: Solid State Phys. **6**, 2105 (1973).

[43] M. Barturen, D. Sander, J. Milano, J. Premper, C. Helman, M. Eddrief, J. Kirschner, and M. Marangolo, Bulklike behavior of magnetoelasticity in epitaxial FeGa thin films, Phys. Rev. B **99**, 134432 (2019).

[44] R. L. Stamps and B. Hillebrands, Dipolar interactions and the magnetic behavior of two-dimensional ferromagnetic systems, Phys. Rev. B **44**, 12417 (1991).